Model-Based Approaches for Channel Charting in Next-Generation Wireless Networks with Large-Scale Antenna Arrays

Yonghong Jiang
University of California, Irvine, CA, USA

Ender Ayanoglu, *Fellow, IEEE*
University of California, Irvine, CA, USA

***Abstract*—Channel charting seeks to infer low-dimensional, geometry-preserving representations of user equipment (UE) locations from high-dimensional channel state information (CSI) measured at a base station (BS). Most existing approaches rely on self-supervised dimensionality reduction or end-to-end neural networks that treat CSI as unstructured data and largely ignore known physical properties of wireless propagation and array geometry. This paper describes a model-based and model-aware framework for channel charting, localization, and spectrum-aware control that explicitly exploits physical channel models, angle-of-arrival (AoA) structure, and classical signal processing algorithms. By integrating analytical methods with learning-based components in a unified architecture, we aim to improve accuracy, robustness, interpretability, and data efficiency. We describe: 1) Employment of real-world measurement data. 2) Neural network-based forward charting function. 3) Rotate-and-sum algorithm for ρ or θ. 4) Channel charting within a multi-cell network. This workshop paper establishes algorithmic foundations for model-aware dimensionality reduction and hybrid inference–control in NextG wireless systems with large-scale antenna arrays.**

***Index Terms*—Multiple signal classification (MUSIC), Bartlett algorithm, Minimum Variance Distortion Response (MVDR or Capon) algorithm, Minimum Norm algorithm.**

I. Introduction

A channel chart is a representation constructed from channel state information (CSI). It possesses the property of preserving the relative geometry of the radio environment, which consists of a base station (BS) and user equipment (UEs) [1]. By leveraging this chart, the BS can infer the relative locations of the UEs. This capability enables a variety of applications, including handover, cell search, and user localization. While most existing works estimate a channel chart using dimensionality reduction techniques, in this paper we instead construct the channel chart directly through model-based approaches.

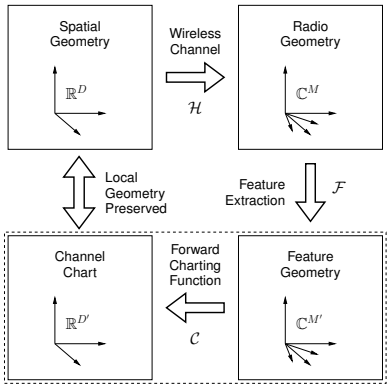

Fig. 1. Summary of channel charting via dimensionality reduction [1].

We begin our discussion with Fig. 1, which is a simplified and redrawn version of [1, Fig. 3]. UE transmitters are located in spatial geometry $\mathbb{R}^D$, where $D = 2$ or 3 [1]. The BS receiver computes CSI in radio geometry $\mathbb{C}^M$, where $M \gg D$. Subsequently, a channel chart is formed in $\mathbb{R}^{D'}$, where $D' \leq D$, such that the representation in $\mathbb{R}^{D'}$ preserves the local geometry of the original spatial locations in $\mathbb{R}^D$, i.e., the relative positions of the UEs. Reference [1] introduces and compares three dimensionality reduction algorithms: principal component analysis (PCA), Sammon's mapping (SM), and autoencoder (AE). PCA is a linear dimensionality reduction technique that maps a high-dimensional point set (e.g., CSI features) into a low-dimensional representation (e.g., the channel chart) in an unsupervised manner. It operates only on the data used during computation and does not yield a mapping function applicable to future data points. Therefore, strictly speaking, it is not a machine learning (ML) algorithm, although it is sometimes categorized as an unsupervised ML method. SM is a nonlinear dimensionality reduction technique that preserves small pairwise distances between points in the two spaces [1]. Similar to PCA, it does not produce a function for processing future data. In contrast, an AE is a deep neural network designed for unsupervised dimensionality reduction [1]. Unlike PCA and SM, it learns a mapping and can therefore be applied to new data points.

Referring again to Fig. 1, four processing blocks are involved in channel charting. The upper-left block represents the spatial geometry in $\mathbb{R}^D$, while the upper-right block corresponds to the radio geometry in $\mathbb{C}^M$, where CSI is computed. The lower blocks perform feature extraction and forward charting to generate the channel chart. In the approach proposed in this paper, we retain the upper two blocks as in [2]–[4]. However, we replace the lower two blocks with model-based techniques that directly estimate the angle of arrival and the distance of each UE from the BS. As a result, the relative positions of the UEs with respect to the BS are preserved, and the fundamental objective of channel charting is inherently achieved.

Algorithm 1 MUSIC Procedure for Estimating θ

Calculate the CSI across antennas and subcarriers covariance matrix $\mathbf{R} = \mathbb{E}[\mathbf{h}\mathbf{h}^H]$
Get the eigenvectors and eigenvalues of $\mathbf{R}$
Separate system subspace $\mathcal{S}$ and noise subspace $\mathcal{N}$ by defining a threshold
Calculate $\mathbf{N}$ by concatenating the eigenvectors of $\mathcal{N}$
for $\theta = 0 : 180$ in increments of 1 **do**
  Calculate the steering vector $\mathbf{A}(\theta)$
  Calculate the PMF$(\theta) = P_{MUSIC}(\theta) = \frac{1}{\text{Norm}_2(\mathbf{N}^H\mathbf{A}(\theta))}$
end for
Search the PMF for a peak and find the corresponding θ

Our past work on this subject includes [2]–[6]. In order to follow the discussion in the sequel, we refer the reader to [1] for the basics of channel charting, definitions of channel models LOS, QLOS, and QNLOS, and the algorithms PCA, SM, and AE, and to [2] for the algorithms ISQ, LR, and MM. In addition to a visual comparison of channel charts, we will use continuity (CT) and trustworthiness (TW) as objective performance measures [1], [2]. CT specifies if neighbors in the original space are close in the representation space. TW measures how well the feature mapping avoids introducing new neighbor relations that were not present in the original space. Point-wise and global CT and TW are between 0 and 1, with larger values being better [1].

II. Algorithms for AoA Estimation

We will discuss four algorithms on AoA estimation from the literature, e.g., [7], [8].

A. MUSIC Algorithm

Let θ be the Angle of Arrival (AoA) for transmission from a UE to a BS with N_R receive antennas. One can compose the steering vector

$$\mathbf{A}(\theta) = (1, e^{j\pi\cos(\theta)}, e^{j\pi 2\cos(\theta)}, \ldots, e^{j\pi(N_R-1)\cos(\theta)})^T. \quad (1)$$

Then, MUSIC is used to determine the AoA θ as in Algorithm 1 where $P_{MUSIC}(\theta)$ is a probability mass function up to a normalization constant.

B. Bartlett's Algorithm

With our earlier definition of the autocorrelation matrix $\mathbf{R}$ and the steering vector $\mathbf{A}(\theta)$, this algorithm computes

$$P_{Bartlett}(\theta) = \frac{\mathbf{A}^H(\theta)\mathbf{R}\mathbf{A}(\theta)}{\mathbf{A}^H(\theta)\mathbf{A}(\theta)} \quad (2)$$

and then finds the maximum of $P_{Bartlett}(\theta)$. For a ULA, the denominator is a constant, and it is sufficient to work with its numerator. After calculation, one searches for the maximum of $P_{Bartlett}(\theta)$ to determine the AoA.

C. MVDR (Capon's) Algorithm

The full name for this algorithm is Minimum Variance Distortionless Algorithm (MVDR). It is also known as Capon's algorithm. Its spatial spectrum $P_{MVDR}(\theta)$, similar to $P_{MUSIC}(\theta)$ or $P_{Bartlett}(\theta)$, is given as

$$P_{MVDR}(\theta) = \frac{1}{\mathbf{A}^H(\theta)\mathbf{R}^{-1}\mathbf{A}(\theta)}. \quad (3)$$

Once again, after calculation, one searches for the maximum of $P_{MVDR}(\theta)$ to determine the AoA.

D. Minimum Norm Algorithm

The Minimum Norm (MN) method uses an eigenspace decomposition of the covariance matrix $\mathbf{R}$ to separate signal and noise subspaces:

$$\mathbf{R} = \mathbf{U}_s\mathbf{D}_s\mathbf{U}_s^H + \sigma^2\mathbf{U}_n\mathbf{U}_n^H \quad (4)$$

where $\mathbf{U}_s$ contains the signal eigenvectors and $\mathbf{U}_n$ the noise eigenvectors. The MN spectrum is

$$P_{MN}(\theta) = \frac{1}{\mathbf{A}^H(\theta)\mathbf{U}_n\mathbf{U}_n^H\mathbf{A}(\theta)}, \quad (5)$$

providing improved resolution compared to non-subspace methods.

III. Simulation Results

In our work [2], we first adopted the MUSIC algorithm to determine the distance between the BS and UE, or the range ρ by using multicarrier modulation. Then, we came to the conclusion that using the MUSIC algorithm for estimating both θ and ρ performed the best among the algorithms studied, including LR and ISQ. We call the resulting algorithm MUSIC/MUSIC, or MM. We show the performance of employing the MM algorithm in Fig. 2. We provide the running times of using the MM algorithm in Table I. We then used the Bartlett algorithm for the same purpose. We show the performance of employing the Bartlett algorithm for estimation of both θ and ρ in Fig. 3. We provide the running times of using the Bartlett algorithm to estimate both θ and ρ in Table II. In implementing the Bartlett algorithm, Cholesky factorization of the autocorrelation matrix $\mathbf{R}$ is made for reduction in computational complexity. From the results presented, clearly the Bartlett algorithm has a substantial reduction in computational complexity without a discernible reduction in the quality of the channel charts or performance measures TW and CT.

IV. Extensions of the Basic Results

Key findings in our previous works [2]–[6] can be summarized as follows:

1) ISQ and LR offer substantially better charting performance than PCA, SM, and AE both visually and in terms of the figures of merit CT and TW [2].
2) We introduced the MM algorithm, which estimates θ using MUSIC and, through our new multicarrier MUSIC technique [2], [4], also estimates ρ. MM outperforms PCA, SM, AE, LR, and ISQ in visual quality as well as CT and TW.

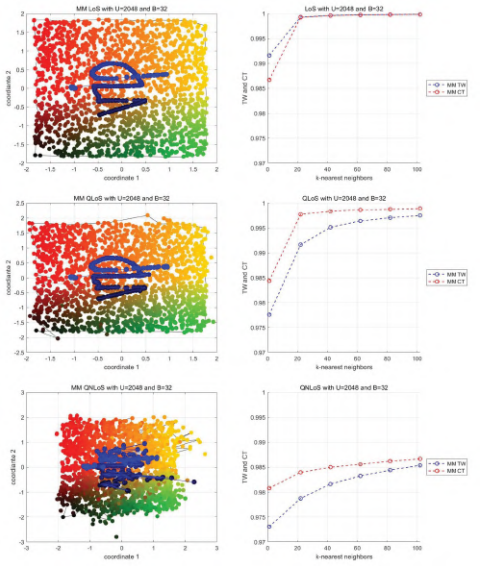

Fig. 2. Channel charts and TW and CT values for employing the MUSIC algorithm to estimate both θ and ρ. Top: LOS, Middle: QLOS, Bottom: QNLOS.

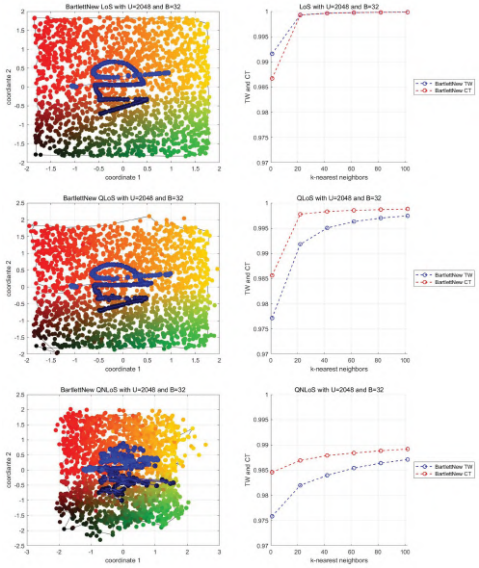

Fig. 3. Channel charts and TW and CT values for employing the Bartlett algorithm to estimate both θ and ρ. Top: LOS, Middle: QLOS, Bottom: QNLOS.

TABLE I
RUNNING TIMES FOR EMPLOYING THE MUSIC ALGORITHM TO ESTIMATE BOTH θ AND ρ.

Channel	Runtime (s)
LOS	20.6577
QLOS	20.6061
QNLOS	20.8503

TABLE II
RUNNING TIMES FOR EMPLOYING THE BARTLETT ALGORITHM TO ESTIMATE BOTH θ AND ρ.

Channel	Runtime (s)
LOS	1.1203
QLOS	1.1407
QNLOS	1.1373

3) We further showed that the Bartlett algorithm, when used to estimate both θ and ρ (BB algorithm), matches the performance of MM while requiring substantially lower execution time.

This paper aims to discuss ways to extend the results in our previous papers in several important directions.

A. Real-World Measurement Data

All of the results we have discussed up to this point were created using simulated data in the form of LOS, QLOS, and QNLOS. Although the data in QLOS and QNLOS models were found to be a good representation of measured data, it is worthwhile to carry out studies by using real-world measured data from the literature. In fact, this was suggested to us during our presentation in the 2024 Asilomar conference. We note that [9] employs a dataset generated by real measurements. It is available from the University of Stuttgart DICHASUS collection at [10]. This is a dataset of CSI data from a massive Multi-Input Multi-Output Orthogonal Frequency Division Multiplexing (MIMO-OFDM) channel sounder, with time and phase synchronization, including "ground truth" positions. Another set includes CSI data from the University of Stuttgart ESPARGOS collection. This is a MIMO-OFDM channel sounder based on Wi-Fi, with phase synchronization, and includes ground truth positions [11]. Yet another dataset is called Fraunhofer UWB and 5G collection [12]. This set is measured in an indoor environment. It includes channel impulse responses and time of flight or time difference of arrival data. It also includes ground truth positions. It is possible to use part of the data in these datasets to verify all of our results in our papers for real-world conditions.

In addition, these real-world datasets naturally capture temporal evolution due to user mobility and environmental dynamics. The use of DICHASUS, ESPARGOS, and Fraunhofer data will enable one to examine how channel charts evolve under realistic time-varying conditions.

We also note that the real-world datasets exhibit non-uniform user densities and varying spatial sampling patterns. This enables one to examine how the quality of the resulting channel charts depends on UE density.

Furthermore, because these measurement datasets include transmissions from heterogeneous user devices with different antenna characteristics, they inherently capture UE-dependent antenna pattern variations. This provides an opportunity to assess the robustness of our methods to device-specific antenna effects without introducing additional modeling assumptions.

B. Neural Network-Based Forward Charting Function

Two broad approaches exist for constructing the Forward Charting Function (FCF) in Fig. 1. The original approach [1] uses dimensionality reduction (PCA, SM, AE). We have already shown that our model-based methods outperform these

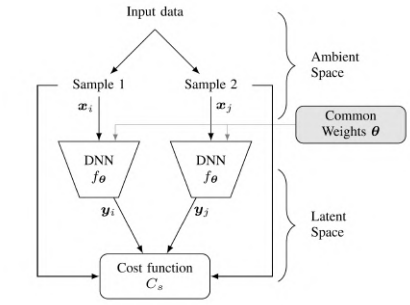

Fig. 4. Structure of a generic Siamese networks architecture. Both deep neural network (DNN) blocks are identical, and use the same weights [13].

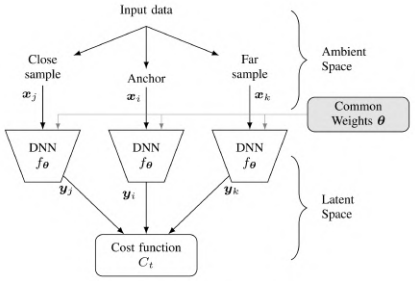

Fig. 5. Triplet network architecture The three DNN blocks are identical, and use the same weights [13].

techniques. The second approach employs neural networks as the FCF.

Early work [14] incorporated side information into an autoencoder, but suffered from poor distance preservation and training difficulty [15]. A more promising solution uses a *Siamese neural network* [15], shown in Fig. 4. Siamese networks map pairs of CSI samples to embeddings and minimize the cost

$$C_s = \frac{1}{|\mathcal{T}|} \sum_{(i,j)\in\mathcal{T}} \left(\|\mathbf{x}_i - \mathbf{x}_j\| - \|\mathbf{y}_i - \mathbf{y}_j\| \right)^2, \qquad (6)$$

which effectively seeks to minimize CT.

Triplet networks [13], shown in Fig. 5, extend this idea using anchor-positive-negative triplets:

$$C_t = \frac{1}{|\mathcal{T}|} \sum_{(i,j,k)\in\mathcal{T}} \left(\|\mathbf{y}_i - \mathbf{y}_j\| - \|\mathbf{y}_i - \mathbf{y}_k\| \right)^+, \qquad (7)$$

where $(x)^+ = \max(x, 0)$.

FCFs based on neural networks are attractive because: *i)* neural networks are powerful function approximators, *ii)* large datasets can be efficiently handled via stochastic gradient descent, and *iii)* side information (e.g., time or frequency structure) can be easily incorporated.

However, these methods remain *data-driven attempts to minimize* CT, whereas our approach leverages explicit physical modeling. We hypothesize that model-based techniques will outperform both Siamese and triplet networks, and testing this hypothesis will provide valuable insight regardless of outcome.

A related work [9] uses Time of Arrival (ToA) or AoA estimates from multiple BSs to assist a Siamese network used as the FCF. Their method requires four BSs and multilateration or triangulation, in contrast to our single-BS framework.

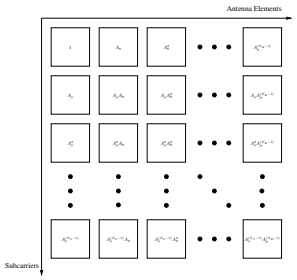

Fig. 6. Ideal CSI matrix $(N_S \times N_R)$ in the absence of fading and noise.

As a summary, it is important to implement Siamese and triplet neural networks for the FCF following [9], [13], [15], and compare them to our model-based methods in terms of visual chart quality, CT, TW, computational complexity, and communication overhead. It will also be likely useful to explore hybrid approaches where neural networks are enhanced by our model-based AoA and ρ estimators.

C. Rotate-and-Sum (RS) Algorithm for ρ or θ

To further reduce computational complexity, we introduced the *rotate-and-sum* (RS) algorithm in [2]. The CSI matrix (Fig. 6) contains N_R receive antennas (columns) and N_S subcarriers (rows). In an ideal noise-free case, adjacent antenna elements differ by a known phase factor $A_\theta = e^{j\pi\cos\theta}$, and adjacent subcarriers differ by $A_\rho = e^{-j2\pi\rho\Delta f/c}$.

For each row vector $\mathbf{c}$ of the CSI matrix, the correlation matrix entry is

$$[\mathbf{c}^H\mathbf{c}]_{i,j} = \begin{cases} A_\theta^{j-i}, & i \le j, \\ (A_\theta^*)^{i-j}, & i > j, \end{cases}$$

which is independent of the row index. Averaging $\mathbf{c}^H\mathbf{c}$ over all rows yields a matrix $\mathbf{S}$ that approximates this ideal structure even in the presence of fading and noise.

To estimate θ, we generate candidate matrices $\mathbf{B}(\phi)$ with $\phi \in [0, \pi]$ and select the ϕ whose $\mathbf{B}(\phi)$ best matches $\mathbf{S}$. An analogous procedure estimates ρ.

The RS algorithm avoids eigenanalysis and thus has significant implementation advantages. Preliminary simulations show that RS performs *very close* to MM across LOS, QLOS, and QNLOS channels [2]. Because RS primarily requires multiply-accumulate operations, it is well suited for Register Transfer Level (RTL) hardware implementation, unlike MUSIC-based methods that often require a DSP core.

Improved measures of similarity between $\mathbf{S}$ and $\mathbf{B}(\phi)$ beyond the simple correlation metric used in [2] can be examined, including various matrix norms and robust measures needed in multiuser or interference-limited settings.

D. Channel Charting Within a Multi-Cell Network

All prior work on channel charting, including [1]–[6], assumes a single isolated cell. In realistic networks, inter-cell interference introduces multiple peaks in the AoA/ρ PMFs.

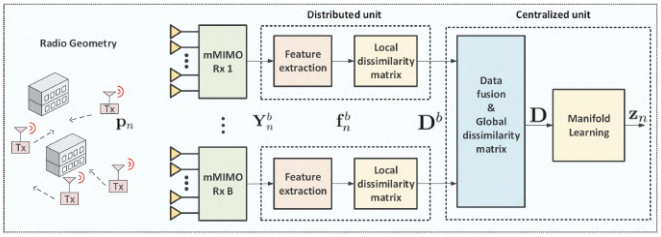

Fig. 7. Multi-point channel charting framework [16].

First, channel charting can be studied independently in each cell using our MM or BB algorithms.

A more general framework is the multipoint channel charting (MPCC) method of [16], illustrated in Fig. 7. Each of B BSs computes local UE-UE dissimilarity matrices, which are then combined into a global matrix and processed using manifold learning methods such as SM, Laplacian eigenmaps, or t-SNE [16]. Their approach estimates AoAs for multiple paths using MUSIC and approximates ρ via $\sqrt{\lambda_i}$, where λ_i is the eigenvalue associated with the ith path. This approximation is ad hoc and may place UEs on reflection surfaces rather than their true locations.

We propose two improvements: *i)* bypassing per-path decomposition altogether and using the MM or BB algorithm directly, justified by their strong performance under QLOS/QNLOS multipath; *ii)* retaining the multipath structure but replacing the approximation $[\cos(\theta_i)/\sqrt{\lambda_i}, \sin(\theta_i)/\sqrt{\lambda_i}]$ with the more accurate coordinates $(\rho_i \cos\theta_i, \rho_i \sin\theta_i)$ using AoA/ρ estimates employing methods such as MM and BB.

V. Extension to Very Large Antenna Arrays

Conventional algorithms for AoA estimation, such as MUSIC, Bartlett, MVDR, and Minimum Norm typically assume far-field propagation, planar wavefronts, and steering vectors that depend only on the AoA. These assumptions are valid when the distance to the source is much larger than the array aperture. However, for very large antenna arrays, the Fraunhofer distance increases significantly, and sources may lie in the radiative near-field (Fresnel region), where the wavefront is spherical rather than planar. As a result, the array response depends on both angle and distance, and conventional AoA estimation algorithms become mismatched.

These algorithms admit natural extensions to near-field scenarios by employing spherical-wave steering vectors that depend jointly on angle and range, instead of steering vectors that depend only on angle as in [2]. Under this formulation, joint angle–range estimation is performed, enabling accurate localization in the radiative near-field of large arrays. Such extensions follow directly from the general array processing framework in [7] and are supported by other work on near-field array processing with spherical-wave models, e.g., [17].

This observation motivates the use of model-based approaches that directly estimate angle and range, thereby avoiding the need for dimensionality reduction in channel charting.

To formalize the near-field model, consider a source located at position $\mathbf{p} \in \mathbb{R}^3$ and an array with sensor positions $\{\mathbf{p}_m\}_{m=1}^M$. Under spherical-wave propagation, the steering vector is given by

$$\mathbf{A}(\mathbf{p}) = \left[e^{-j\frac{2\pi}{\lambda}\|\mathbf{p}-\mathbf{p}_1\|}, \ldots, e^{-j\frac{2\pi}{\lambda}\|\mathbf{p}-\mathbf{p}_M\|}\right]^T. \quad (8)$$

Accordingly, near-field localization can be formulated as a search over $\mathbf{p}$, e.g., via

$$\hat{\mathbf{p}} = \arg\max_{\mathbf{p}} f\big(\mathbf{A}(\mathbf{p}), \mathbf{R}\big), \quad (9)$$

where $f(\cdot)$ denotes the objective function associated with a given algorithm (e.g., MUSIC, Bartlett, MVDR, or Minimum Norm) and $\mathbf{R}$ is the sample covariance matrix; e.g., $f = 1/(\mathbf{A}^H(\mathbf{p})\mathbf{R}^{-1}\mathbf{A}(\mathbf{p}))$ for MVDR. It should be noted that $\mathbf{p}$ depends on both the AoA and the range and the operation in (9) is a scan over both the AoA and the range, as opposed to only the AoA in the case of the far-field approximation of Section II.

References

[1] C. Studer, S. Medjkouh, E. Gonultas, T. Goldstein, and O. Tirkkonen, "Channel charting: Locating users within the radio environment using channel state information," *IEEE Access*, vol. 6, pp. 47 682–47 698, 2018.

[2] A. Aly and E. Ayanoglu, "Model-based approaches to channel charting," *IEEE Transactions on Communications*, vol. 72, no. 2, pp. 1207–1222, Feb. 2024.

[3] ——, "Estimation of cellular wireless user coordinates via channel charting and MUSIC," in *2023 International Conference on Computing, Networking and Communications (ICNC)*, 2023, pp. 343–347.

[4] ——, "Channel charting: Model-based approaches," in *ICC 2023 - IEEE International Conference on Communications*, 2023, pp. 1054–1060.

[5] Y. Jiang and E. Ayanoglu, "Alternative channel charting techniques in cellular wireless communications," in *2024 58th Asilomar Conference on Signals, Systems, and Computers*, Oct. 2024, **Invited Paper**.

[6] ——, "Alternative channel charting techniques in cellular wireless communications," preprint, arXiv:2412.13217, Dec. 2024.

[7] H. L. Van Trees, *Optimum Array Processing: Part IV of Detection, Estimation, and Modulation Theory*. Wiley, 2002.

[8] H. Krim and M. Viberg, "Two decades of array signal processing research: The parametric approach," *IEEE Signal Processing Magazine*, vol. 13, no. 4, pp. 67–94, 1996.

[9] F. Euchner, P. Stephan, and S. ten Brink, "Augmenting channel charting with classical wireless source localization techniques," in *2023 57th Asilomar Conference on Signals, Systems, and Computers*, 2023, pp. 1641–1647.

[10] University of Stuttgart, "DICHASUS Data Set," `dichasus.inue.uni-stuttgart.de`.

[11] ——, "ESPARGOS Data Set," `espargos.net/datasets`.

[12] Fraunhoffer, "UWB and 5G Data Set," `channelcharting.github.io`.

[13] P. Ferrand, A. Decurninge, L. G. Ordonez, and M. Guillaud, "Triplet-based wireless channel charting: Architecture and experiments," *IEEE J. Sel. Areas Commun.*, vol. 39, no. 8, pp. 2361–2373, 2021.

[14] P. Huang, O. Castaneda, E. Gonultas, S. Medjkouh, O. Tirkkonen, T. Goldstein, and C. Studer, "Improving channel charting with representation-constrained autoencoders," in *2019 IEEE 20th International Workshop on Signal Processing Advances in Wireless Communications (SPAWC)*, 2019, pp. 1–5.

[15] E. Lei, O. Castaneda, O. Tirkkonen, T. Goldstein, and C. Studer, "Siamese neural networks for wireless positioning and channel charting," in *2019 57th Annual Allerton Conference on Communication, Control, and Computing (Allerton)*, 2019, pp. 200–207.

[16] J. Deng, S. Medjkouh, N. Malm, O. Tirkkonen, and C. Studer, "Multipoint channel charting for wireless networks," in *2018 52nd Asilomar Conference on Signals, Systems, and Computers*, 2018, pp. 286–290.

[17] B. Friedlander, "Localization of signals in the near-field of an antenna array," *IEEE Transactions on Signal Processing*, vol. 67, no. 15, pp. 3885–3893, 2019.